Pushing the Limits of Functionality-Multiplexing Capability in Metasurface Design Based on Statistical Machine Learning

Wei Ma,* Yihao Xu, Bo Xiong, Lin Deng, Ru-Wen Peng,* Mu Wang, and Yongmin Liu*

As 2D metamaterials, metasurfaces provide an unprecedented means to manipulate light with the ability to multiplex different functionalities in a single planar device. Currently, most pursuits of multifunctional metasurfaces resort to empirically accommodating more functionalities at the cost of increasing structural complexity, with little effort to investigate the intrinsic restrictions of given meta-atoms and thus the ultimate limits in the design. In this work, it is proposed to embed machine-learning models in both gradient-based and nongradient optimization loops for the automatic implementation of multifunctional metasurfaces. Fundamentally different from the traditional two-step approach that separates phase retrieval and meta-atom structural design, the proposed end-to-end framework facilitates full exploitation of the prescribed design space and pushes the multifunctional design capacity to its physical limit. With a single-layer structure that can be readily fabricated, metasurface focusing lenses and holograms are experimentally demonstrated in the near-infrared region. They show up to eight controllable responses subjected to different combinations of working frequencies and linear polarization states, which are unachievable by the conventional physics-guided approaches. These results manifest the superior capability of the data-driven scheme for photonic design, and will accelerate the development of complex devices and systems for optical display, communication, and computing.

1. Introduction

Different from bulk metamaterials, metasurfaces consist of 2D planar arrays of artificially engineered subwavelength structures, the so-called meta-atoms.[1–3] Empowered by the delicately designed structure and distribution of meta-atoms, the burst of metasurface research has spawned new types of flat optical components including beam deflectors,[4] high-quality-factor diffractors,[5] wave plates,[6] lenses,[7,8] and holograms.[9,10] Compared with their bulky counterparts that often rely on the phase accumulation of light propagating through conventional media, metasurface-based components can efficiently manipulate light by a deep subwavelength interface, making them compact, easy for integration, and relatively low loss, especially when dielectric materials are used.[11] In addition, the large flexibility in metasurface design offers unique ability to control light for multipurposed tasks that are usually inaccessible based on natural materials, yielding prescribed optical responses to different combinations of light characteristics such as the frequency, phase, angle of incidence, and polarization.[12–20]

The exotic optical properties of metasurfaces originate from the engineered light–structure interactions. The conventional design approach heavily relies on template-based parameter sweep via numerical simulations to find eligible meta-atom structures, which could be facilitated by physical principles such as plasmonic resonance,[21] Mie theory,[22] or Pancharatnam–Berry (PB) phase for circular polarized light.[23] In the case of multifunctional metasurfaces, the design routines often utilize an empirical decoupling of the meta-atom response using multimode resonance in dielectric pillars,[24]

W. Ma
State Key Laboratory of Modern Optical Instrumentation
College of Information Science and Electronic Engineering
Zhejiang University
Hangzhou 310027, China
E-mail: ma_wei@zju.edu.cn
Y. Xu, Y. Liu
Department of Mechanical and Industrial Engineering
Northeastern University
Boston, MA 02115, USA
E-mail: y.liu@northeastern.edu

B. Xiong, R.-W. Peng, M. Wang
National Laboratory of Solid State Microstructures
School of Physics
and Collaborative Innovation Center of Advanced Microstructures
Nanjing University
Nanjing 210093, China
E-mail: rwpeng@nju.edu.cn
L. Deng, Y. Liu
Department of Electrical and Computer Engineering
Northeastern University
Boston, MA 02115, USA

**ADVANCED
SCIENCE NEWS**

www.advancedsciencenews.com

**ADVANCED
MATERIALS**

www.advmat.de

combination of PB phase and resonant phase,[25,26] or spatially multiplexing single-responsive meta-atoms in segment,[27] interleaving,[28] or vertical stacking[29] configurations. Such design schemes usually fail to fully exploit the design space and become less practical as the number of multiplexed functionalities increases. Some inverse design algorithms,[30] including gradient-based techniques such as adjoint method[31–34] or heuristic approaches like genetic algorithm,[35,36] may be effective in some multitarget optimization problems of metasurfaces. However, gradient-based design algorithms are prone to be stuck in unsatisfactory local optimum, while heuristic optimization algorithms often require formidable amount of numerical simulation that is impractical for large design space.

Very recently, deep learning and, more generally, statistical machine learning have revolutionized artificial intelligence researches by continuously pushing the state of the art of many traditional pattern recognition tasks, such as computer vision and natural language processing.[37] The accompanying data-driven modeling has also produced powerful analytical tools in material sciences[38] and also new design paradigms for metamaterials.[39,40] Different from the conventional inverse design methods that manage to explore the design space following certain rules, deep learning models automatically learn the complex relationships between distinct photonic structures and their optical responses from sampled training data in the design space. Under such a data-driven approach, various deep learning models have been introduced in metamaterial design problems including multilayer perceptrons,[41–45] convolutional neural networks (CNNs),[46] generative adversarial networks,[47–49] and variational autoencoders (VAE).[50–52] Well trained on precollected data, these delicately constructed deep learning models can produce meta-atoms upon given optical requirements with high efficiency, fidelity, and diversity. By further pairing deep learning with genetic algorithms,[53,54] topology optimization,[55] or adjoint optimization,[56] the meta-atoms generated by deep learning models can be refined with improved performance or assembled in fully functional metasurface devices.

In this work, we conceptually propose a statistical perspective to estimate the design capability of multifunctional metasurfaces and, consequently, demonstrate an end-to-end design pipeline to experimentally realize such physically limited optimal design in a given parameter space. So far, the multifunctional metasurface design, with either conventional parameter sweeps or algorithm-based inverse methods,[54] has followed a two-step, top-down design strategy. First, the design targets are manually decoupled into several subfunctions, and the ideal optical response distribution on the metasurface plane is retrieved. Subsequently, a finite number of meta-atom representatives are designed to approximate the discretized phase and amplitude values. These approaches isolate the retrieval of required optical response distribution on metasurfaces and the design of individual meta-atoms, which can hardly scale up as the number of design targets and thus the complexity of the required meta-atom response increases. In contrast, we resort to statistical machine learning as the bridge that directly links the structural parameters of each single meta-atom and the target metasurface performance. The machine-learning model is composed of several probabilistic inverse retrieving models and a deterministic predicting model, which accurately capture and faithfully reproduce the statistical features of the high-dimensional joint distribution of meta-atom structures and their optical responses. Consequently, instead of artificially decoupling the complex optical response into independent subtargets,[57] a system-level multiobject optimization can be implemented by embedding the proposed machine-learning models in an end-to-end design loop with other algorithms according to specific metasurface functionalities. This design scheme, considering the nonideal meta-atom responses in an automatic optimization process, can fully exploit the design space to push the design capacity to its physical limit. For the first time, without involving spatial multiplexing or PB phase, multifunctional metasurface lenses and holograms are demonstrated, which show up to eight distinct optical responses upon different combinations of frequencies and polarizations. Our design strategy and experimental demonstration will stimulate continual efforts of applying machine learning and other artificial intelligence techniques to transform the areas of optical design, integration, and measurement.

2. Results and Discussions

2.1. Metasurface Design Pipeline

We focus on metasurfaces operating in the reflective configuration as a specific example. The statistical machine-learning model consists of a forward model that predicts reflection spectra from meta-atom design parameters, and an inverse model that retrieves possible meta-atom geometries from given phase requirements on the reflection spectra. From the perspective of a designer, the forward prediction of optical responses should be complete and accurate, including both amplitude and phase spectra with sufficient spectral resolution to capture all detailed features, while the inverse design of meta-atoms usually focuses on the phase response at a few specific frequencies and polarization states. Therefore, to account for such practical considerations, we construct both models based on deep neural networks (DNNs) but with different strategies. For the predicting model, we use a delicately designed deep architecture to deterministically model the mapping from the design parameters to reflection spectra, while the retrieving model, which targets the one-to-many mapping from the given phase requirements to possible design candidates, is constructed as a stochastic generative model with light-weighted encoder–decoder configuration. The meta-atom under investigation is a reflective metal–insulator–metal (MIM) structure with three coupled rectangular resonators (CRR) on top, which supports pronounced and tunable plasmonic modes by varying the dimensions and separation distances of each rectangular component (nine geometric parameters in our case). This kind of meta-atoms has been utilized to expand the design flexibility in previous works such as controlling the dispersive response of the metasurface.[25,58] The machine-learning models are constructed to bidirectionally link the nine design parameters with the optical responses. We use a residual connection configuration with a hybrid CNN and recurrent neural network (RNN) as predicting network, while the retrieving network is a
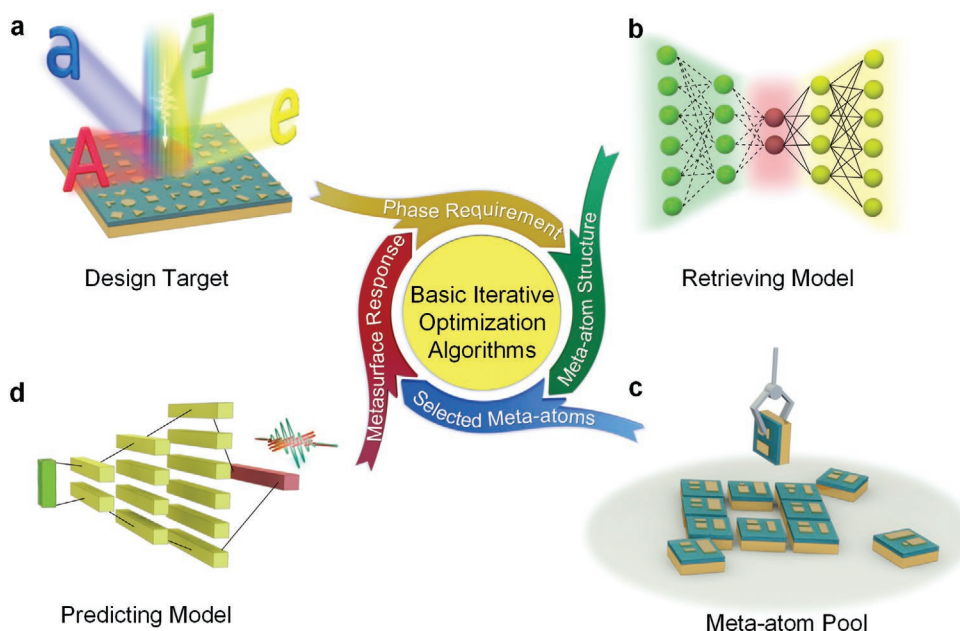
Figure 1. End-to-end design pipeline for multifunctional metasurfaces. a) From the prescribed design target, b) the retrieving model stochastically generates c) the meta-atom design pool containing potential meta-atom candidates from given phase requirements, while d) the predicting model calculates the optical response of each meta-atom to evaluate the device performance. The two machine-learning models are embedded in user-specified iterative optimization algorithms, allowing bidirectional information flow directly between the optical design target and the structural parameters of metasurface.

VAE-based generative model. The details on the parameterization of the meta-atoms and the optical performances, architecture and training setup of the machine-learning models can be found in Sections S1–S3 (Supporting Information).

After the machine-learning model for meta-atoms is established, the well-trained retrieving model and predicting model can be seamlessly embedded in a complete design and optimization loop for fully functional metasurfaces, as schematically illustrated in **Figure 1**. A typical design process of a metasurface starts with a specific single design target or multiple design targets like versatile wavefront control functionalities under different incident conditions (Figure 1a). The design target will impose a required phase distribution on the metasurface plane, which determines the ideal optical response of each meta-atom. We would like to emphasize that it is not a trivial inverse problem to find the optimal structural parameter of a meta-atom from the desired phase response, especially in the case of multiple frequencies and polarizations. More often than not, it is even harder to estimate whether a physically feasible meta-atom structure exists for a given phase requirements or how such phase requirements can be better approximated with all the degrees of freedom in the design space. Armed with the retrieving model (Figure 1b), we can obtain a set of diversified meta-atom designs for each phase requirement, forming a meta-atom design pool (Figure 1c) for further selection. Since the retrieving model statistically reproduces the distribution of design parameters conditioned on phase requirements, the stochastically generated designs in the meta-atom pool are candidates that match or partially match the ideal phase requirements to the greatest extent. Then these candidates are fed to the predicting model (Figure 1d) that produces their

precise amplitude and phase spectra. The amplitude and phase obtained from the deterministic predicting model are used to evaluate the design targets of the metasurface.

In conventional metasurface design processes, some user-specified optimization algorithms, like gradient descent based on diffraction integral or the Gerchberg–Saxton (GS) algorithm for holograms, are often employed to iteratively update the amplitude and phase distribution on the metasurface for optimal solution. However, these algorithms only optimize the optical response distribution, unable to directly modify the underlying meta-atom design parameters accordingly in an ab initio manner. Other heuristic optimization algorithms, like genetic algorithm or particle swarm algorithm, often require time-consuming numerical simulation to evaluate the target and are also quite sensitive to the initial value. Here, with the proposed machine-learning models embedded in the optimization iteration, the modifications of the amplitude and phase distribution on a metasurface can further backpropagate to update the meta-atom pool in either gradient-based or non-gradient-based methods. Even though in many cases, especially for multifunctional devices, the ideal optical response is not realizable by a physical meta-atom design, the proposed end-to-end design scheme will exploit the whole design space to better approximate the ideal response and push the device performance to its physical limit.

2.2. Evaluation of the Statistical Machine-Learning Model

To have a concrete idea about the design capacity and limitation of the CRR meta-atom, we first inspect the distribution of the

complex reflection coefficients at certain frequencies. Here we employ frequency unit instead of wavelength to be consistent with the data collection procedure using frequency-domain solvers (see the "Experimental Section" for details). We pick a reference frequency of 270 THz and five comparing frequencies of 280, 300, 320, 350, and 400 THz. The complex reflection coefficients for x-polarized incidence at these six frequencies in the entire test dataset are scattered as red dots in the top complex planes of **Figure 2**a. For each frequency, the phases of the reflection coefficients cover a full range of 2π while the amplitudes are mostly concentrated from 0.8 to 1. It means that at each single frequency, by tuning the design parameters, almost any specific phase value can be achieved with high reflection. Alongside the test data, we use our machine-learning model to generate some additional data by randomly sampling a phase value between 0 and 2π. Subsequently, the sampled phase requirements are fed to the retrieving model to find eligible meta-atom designs, and the complex reflection coefficients are obtained by the predicting model, plotted as blue scatter points in the bottom panels of Figure 2a. The test data and model generated data show very good consistency in data distribution, manifesting the capability of our model to reproduce the statistical features of the high-dimensional reflection spectra. To illustrate the correlation in optical responses at different frequencies, we further confine the reflection coefficient at 270 THz in a sector from 0 to $\pi/3$, and plot the distribution of test data and model generated data in Figure 2b. Apparently, for the meta-atoms showing the restrained phase variation at 270 THz, the reflection phase at some adjacent frequencies like 280 and 300 THz also appear to be bounded in certain ranges. However, such characteristics gradually fade out as the frequency increases. Little constraint is observed for the reflection coefficients at the two distant frequencies of 350 and 400 THz, which show almost 2π phase coverage same as the unbounded case in Figure 2a.

As noted above, although the reflection values from all the meta-atoms can cover a 2π phase range at a single frequency, the optical responses of individual meta-atoms at different frequencies are correlated, governed by the complex resonant features of the CRR meta-atom. Intuitively, due to the continuous nature of optical spectra, the reflection at two nearby frequencies should have larger interdependence than that at two frequencies far apart. To quantitatively describe the interdependence among different frequencies and better illustrate the potency of the proposed statistical machine-learning model, we introduce mutual information (MI) of the complex reflections at two frequency points. Mutual information of a pair of random variables is defined as the Kullback–Leibler divergence of their joint distribution and the product of their marginal distributions, which equals zero if and only if the two random variables are independent. We estimate the mutual information for every pair of frequencies from 250 to 400 THz in a nonparametric way using a k-nearest-neighbor-based estimator on all collected data.[59] The results are shown in Figure 2c for both x- and y-polarizations. Consistent with our intuition, the complex reflection exhibits strong interdependence when two frequencies are close to each other. The mutual information value for the five comparing frequencies in Figure 2a,b with respect to the reference frequency of 270 THz is annotated by

the crossmarks along the white dashed line for x-polarization. Clearly, as the target frequency moves farther away from the reference of 270 THz, the mutual information between the two optical responses drops drastically. Another observation from the mutual information plot is that, at higher frequencies, the overall mutual information between a given frequency point and its near neighbors decreases, implying that one can achieve better control of the optical response of a multifrequency metasurface in higher frequency ranges.

To design specific multifunctional metasurfaces, we select four frequency values of 270, 350, 375, and 400 THz, which are assembled into three different design cases for both x- and y-polarizations, namely two-frequency case (350 and 400 THz), three-frequency case (270, 350, and 400 THz), and four-frequency case (270, 350, 375, and 400 THz), respectively. To quantitatively estimate the difficulty of each multifunction design task with certain target frequency values, we calculated mutual information of the complex reflection coefficients over all pairs of adjacent frequencies in the selected target frequency values. Then these mutual information values are averaged, as plotted by blue circles in Figure 2d. Meanwhile, given the number of target design frequencies, we can iteratively search all possible frequency combinations in Figure 2c to find the minimum achievable average mutual information as calculated above. It forms a lower bound that quantitatively describes the interfunctional crosstalk for multifrequency and dual-polarization metasurfaces (red squares in Figure 2d). Details on the minimum achievable mutual information and the corresponding frequency conditions can be found in Section S4 (Supporting Information). Not surprisingly, as the number of target design frequency increases, the average mutual information also increases, meaning stronger interdependence among the optical responses. Roughly according to the scatter plots in Figure 2b and the annotated mutual information in Figure 2c, for frequencies above 350 THz (with 270 THz as reference) or mutual information below 1.73, the interdependence between two frequency points will not destroy the 2π phase tuning range. Back to the design problem of multifunctional metasurfaces, when the number of target design frequencies exceeds five with minimum achievable average mutual information above 2, controllable multifunctional responses is prohibitive due to the strongly interdependent response of meta-atoms at different frequencies. It should be noted that the mutual information value is estimated from data and should not be regarded as an absolute measure in all cases. Nevertheless, it reflects the relative degree of interdependence of the optical responses at different frequencies. More discussions on the mutual information value and the corresponding interdependent distribution of complex reflection coefficients can be found in Section S5 (Supporting Information).

The interdependence of the meta-atom response at different frequencies can be more straightforwardly illustrated by calculating the phase errors between random design targets and model predictions. A random phase requirement is defined and fed to the retrieving model, which can generate a meta-atom candidate. Then the full reflection spectra are obtained by the predicting model. The average discrepancy between the phase of the designed meta-atom and the predefined phase requirements is calculated as the phase error. Apparently, this phase
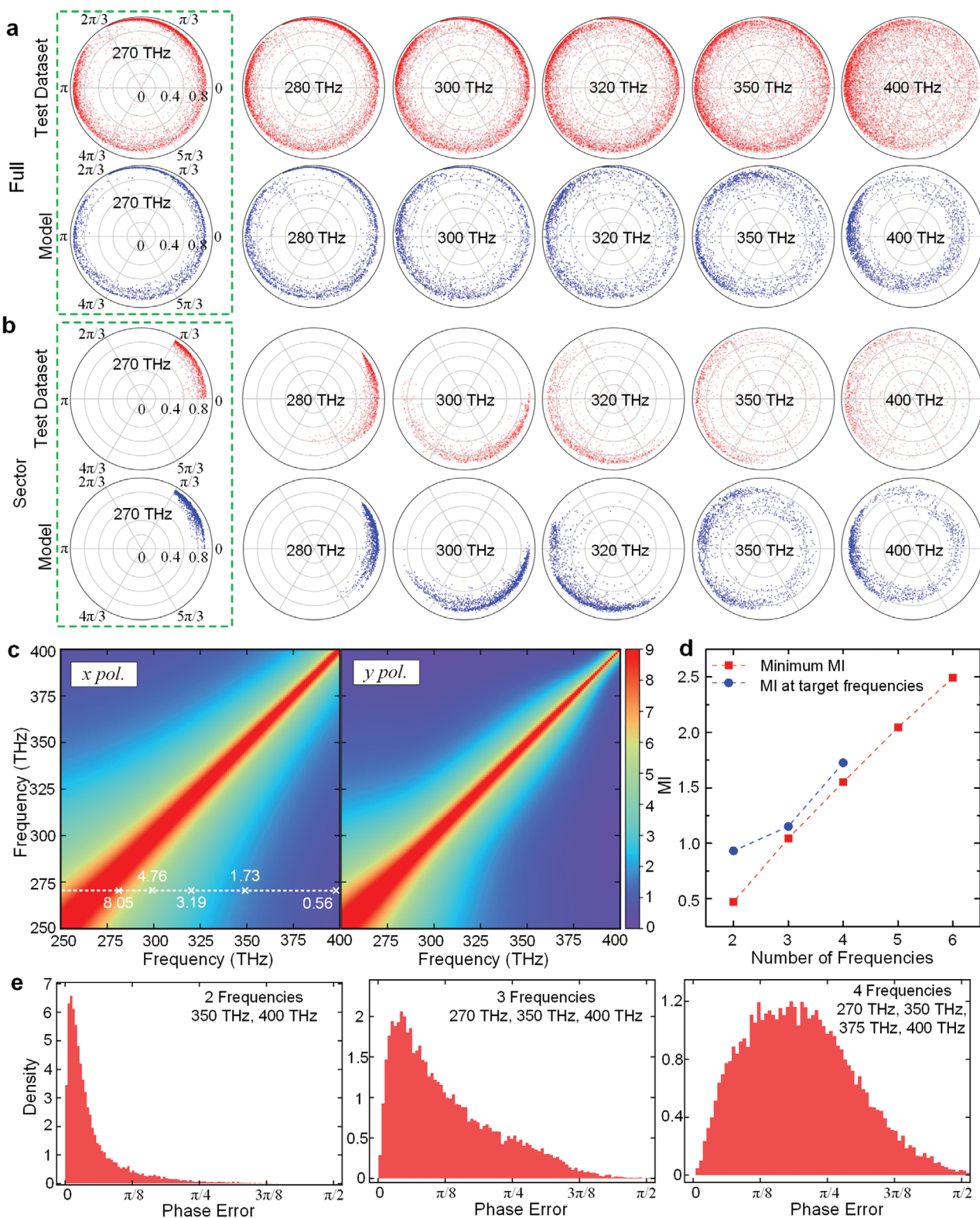
**ADVANCED
SCIENCE NEWS**

www.advancedsciencenews.com

**ADVANCED
MATERIALS**

www.advmat.de

Figure 2. Polar plots of the complex reflection coefficient distribution in the test dataset and in the model-generated dataset at specific frequencies. a) The full distribution of data with selected phase range covering entire 2π. b) The distribution of data when restricting the reflection phase at 270 THz from 0 to $\pi/3$, showing the interdependence among different frequencies. The outer circular boundary in the polar plots stands for reflection amplitude of 1. c) Mutual information (MI) estimated from training data between any two complex reflections in the frequency range of interest. d) Minimum achievable average mutual information as a function of the number of frequencies, in comparison with the mutual information for the three cases in our metasurface design. e) The histograms of phase errors between random design targets and model predictions for different number of frequency points for our device design.

ADVANCED
SCIENCE NEWS
www.advancedsciencenews.com

ADVANCED
MATERIALS
www.advmat.de

error indicates how accurate a given phase requirement can be physically realized, namely, the design limitation of the CRR-based meta-atom for phase control. We have randomly sampled 10 000 phase requirements for each case with two, three, or four frequencies of interest, and the error distribution averaged over two polarization states is plotted as histograms in Figure 2e. Consistent with the mutual information trend in Figure 2d, with the increasing number of required frequency points, the overall phase error also rises. For the two-frequency case, most retrieved phase errors are below $\pi/8$, meaning that the CRR meta-atom can rather independently tune the phase responses at two frequencies. When the frequency number reaches four, the physical intercoupling among different frequencies pushes the average phase error near $\pi/4$ for randomly generated phase requirements. Some of the retrieved meta-atom designs at specific phase requirements for two, three, or four frequencies are given in Section S6 (Supporting Information). These inverse design results verify the potency of our machine-learning model. It produces highly eligible designs if the phase requirements are realizable by the CRR meta-atom, or partially eligible designs that meet the phase requirements to the largest extent for phase targets beyond the optical response constraint of the CRR meta-atom, especially for the four-frequency cases.

2.3. Design and Experimental Demonstration of Multifunctional Metasurface

As discussed in the preceding section, the inherent interdependence of the reflection coefficients at different frequencies and thus the entanglement among different functionalities is the primary barrier in designing multifunctional metasurfaces. Conventional solutions to this problem aim at manually decoupling each individual function, followed by either combining different phase tuning mechanisms or spatially multiplexing simple functionality-specific meta-atoms. Owing to the proposed machine-learning model that captures the statistical features of the design parameters and the corresponding optical responses with both predicting capability and retrieving capability, we can circumvent any empirical human intervention that prevents global optimization or exotic functionalities of the device. Consequently, we are able to realize multifunctional metasurfaces with sophisticated performance unachievable before.

The first prototype device is a multifunctional lens that can focus reflected light with different combinations of polarizations and frequencies at different spatial locations. As shown in **Figure 3**a, the design process starts from retrieving the ideal phase map by reversing the propagation of light from the target focal point to a specific point on the metasurface plane for each individual incident condition. Then the phase requirements are directly fed to the retrieving model to produce an initial metasurface design (dashed arrows), without the need to decouple individual functionalities. Subsequently, the optical response of every single meta-atom on the metasurface is calculated by the predicting model, from which the target function can be evaluated by the focal intensity at each focal point through diffraction integral. As indicated by the solid arrows, gradient descent optimization can be readily performed through the fully differentiable path of the predicting model and diffraction integral.

During the optimization loop, we keep the weights in the neural networks fixed and calculate the gradients of the target function with respect to all the design parameters on the entire metasurface. The gradient information can efficiently guide the optimization process to improve the device performance. As for the target function, we devise a function of the intensity at each focal point, and account for both single point intensity and the balance among different focal points. More details about the choice of target function and the gradient descent optimization of the metasurface focusing lenses are described in Section S7 (Supporting Information).

To experimentally verify our design, we fabricated three focusing lenses working at two frequencies (350 and 400 THz), three frequencies (270, 350, and 400 THz), and four frequencies (270, 350, 375, and 400 THz), respectively. All the devices have a dimension of 100 μm × 100 μm and a vertical focal distance of 200 μm, where the transverse locations of the focal points are offset along either the x- or y-direction by 30 μm for different frequency–polarization combinations, as indicated by the schematic of the target function in Figure 3a. The theoretically calculated and experimentally measured intensity distributions of the reflected light on a cut plane of 200 μm away from the metasurface are presented in Figure 3b–d for each device. The experimental setup for metasurface measurement is described in Section S8 (Supporting Information). It is clear that all the metasurface lenses realize the designed functionalities, and the measured focusing results are in good agreement with the calculation. We also notice that, as the number of target frequencies increases, crosstalk begins to appear between different functionalities, especially for the four-frequency metasurface. This observation is naturally evident given the phase retrieving error and the average mutual information among frequency points in Figure 2, indicating a stronger inherent interdependence as the number of target frequencies increases. Albeit more than one hotspot can be observed in some experimental results (e.g., 350 and 375 THz cases in Figure 3d), the light intensity at the designed focal point is always much higher than those unwanted hotspots caused by crosstalk between working frequencies.

It should be noted that the conventional two-step, top-down design approach can hardly tackle this multipurposed design task. Let us consider discretizing the phase response into eight bins with a $\pi/4$ step, comparable with the average phase error for the four-frequency case in Figure 2e. A four-frequency dual-polarization design requires over 16 million (= 8^8) meta-atom candidates, while even a three-frequency dual-polarization case needs 262 144 (= 8^6) meta-atom candidates to cover all the possible discretized phase requirements on the metasurface. Such a huge number of meta-atom candidates are prohibitive to be prepared by a conventional iterative sweep over the nine design parameters. From the perspective of the design parameters, if a grid search is made over the nine design parameters with a very sparse sampling number of 4 for each parameter, there will be over 260 000 trials to evaluate, far more than the total 70 000 data that we collected to train the machine-learning model. Therefore, traditional brute-force search of meta-atoms is not feasible for multifunctional metasurface design with a large number of design parameters or target functionalities. In contrast, aided by the statistical learning model, we can fully exploit the design space beyond the capability of traditional
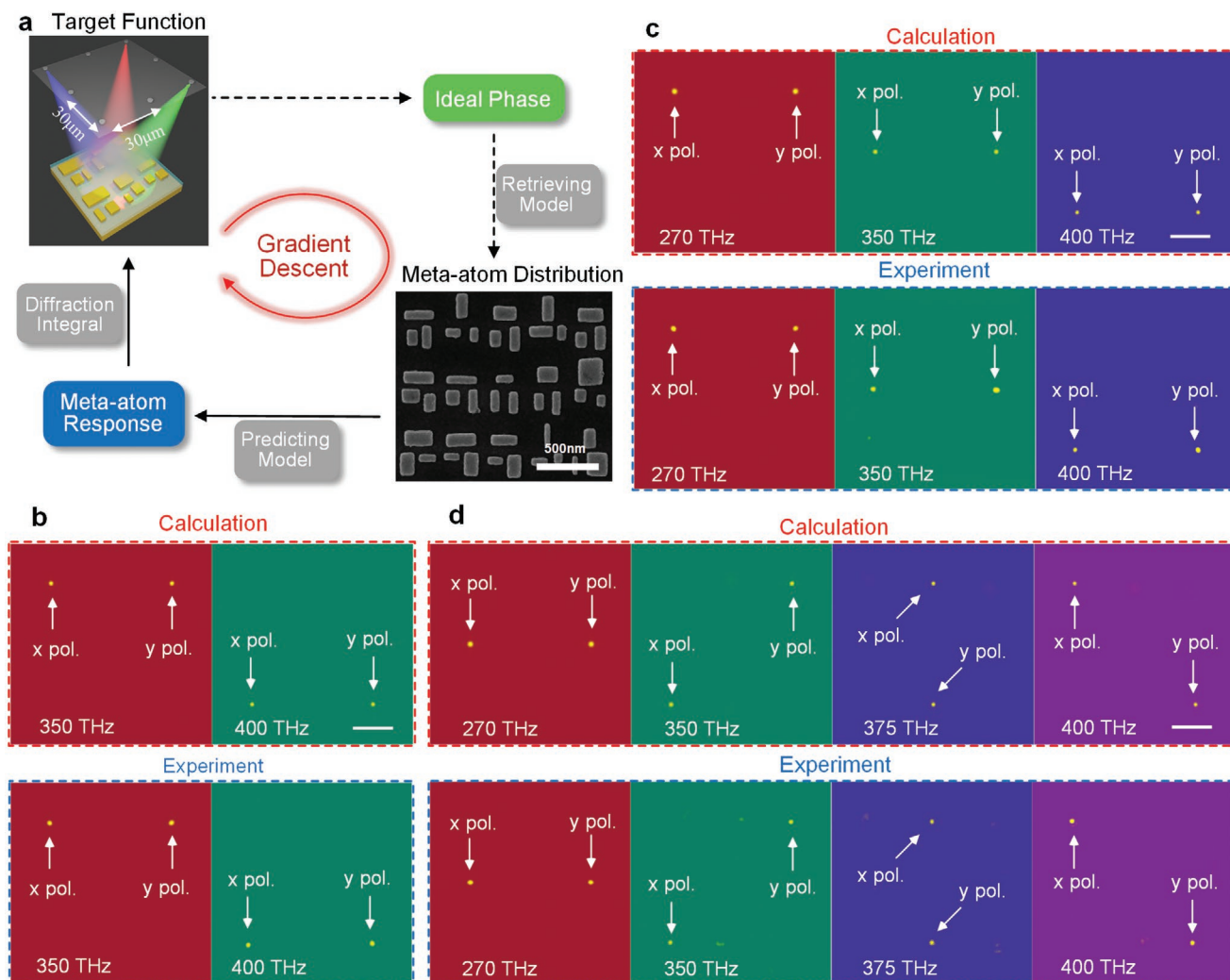
Figure 3. Multifunctional focusing lenses realized by embedding the statistical machine-learning model in a gradient-based optimization loop. a) Flowchart of the design and optimization process, with one scanning electron microscopic image of the fabricated device. The dashed arrows stand for initialization step. b–d) The calculated and experimentally measured focusing results for the two-frequency device (b), the three-frequency device (c), and the four-frequency device (d). The scale bars in the calculated intensity map stand for 20 μm.

methods to achieve up to eight different functionalities. As mentioned before, some of the phase requirements can only be partially realized due to the physical design constraints of the meta-atoms. In order to further push the design capacity to limit, the machine-learning model is embedded in the gradient descent optimization loop, which improves the overall device performance by over 10% compared with the initial design (see Figure S5 in the Supporting Information).

Besides gradient-based optimization, the proposed statistical machine-learning model can also be flexibly embedded in other nongradient iterative optimization algorithms. As depicted in **Figure 4**a, the retrieving model and predicting model are embedded in the GS algorithm for multifunctional metasurface holograms. The conventional GS algorithm approximates the light diffraction by fast Fourier transformation (FFT) and employs an iterative process of FFT followed by inverse FFT (IFFT) to calculate the required phase distribution of a phase-only hologram for the target image. The GS algorithm is a

nongradient optimization process that updates the required phase distribution while forcing a unit amplitude in each iteration. After inserting the proposed statistical learning models in the optimization loop, the retrieved ideal phase in each iteration is mapped to a physical meta-atom design by the retrieving model. The actual optical response, which may deviate from the ideal case, is calculated by the predicting model to estimate the reconstructed target images. Therefore, by linking the design and physical domains, the proposed machine-learning model enables us to consider the nonideal phase retrieval, which may become severe especially in the case of multifunctional metasurface holograms generating distinct images under different illumination conditions.

Similar to multifunctional lenses, we fabricated three multifrequency dual-polarization metasurface holograms working at two frequencies (350 and 400 THz), three frequencies (270, 350, and 400 THz), and four frequencies (270, 350, 375, and 400 THz), respectively. As shown in Figure 4b–d, we use letters "A",

**ADVANCED
SCIENCE NEWS**

www.advancedsciencenews.com

**ADVANCED
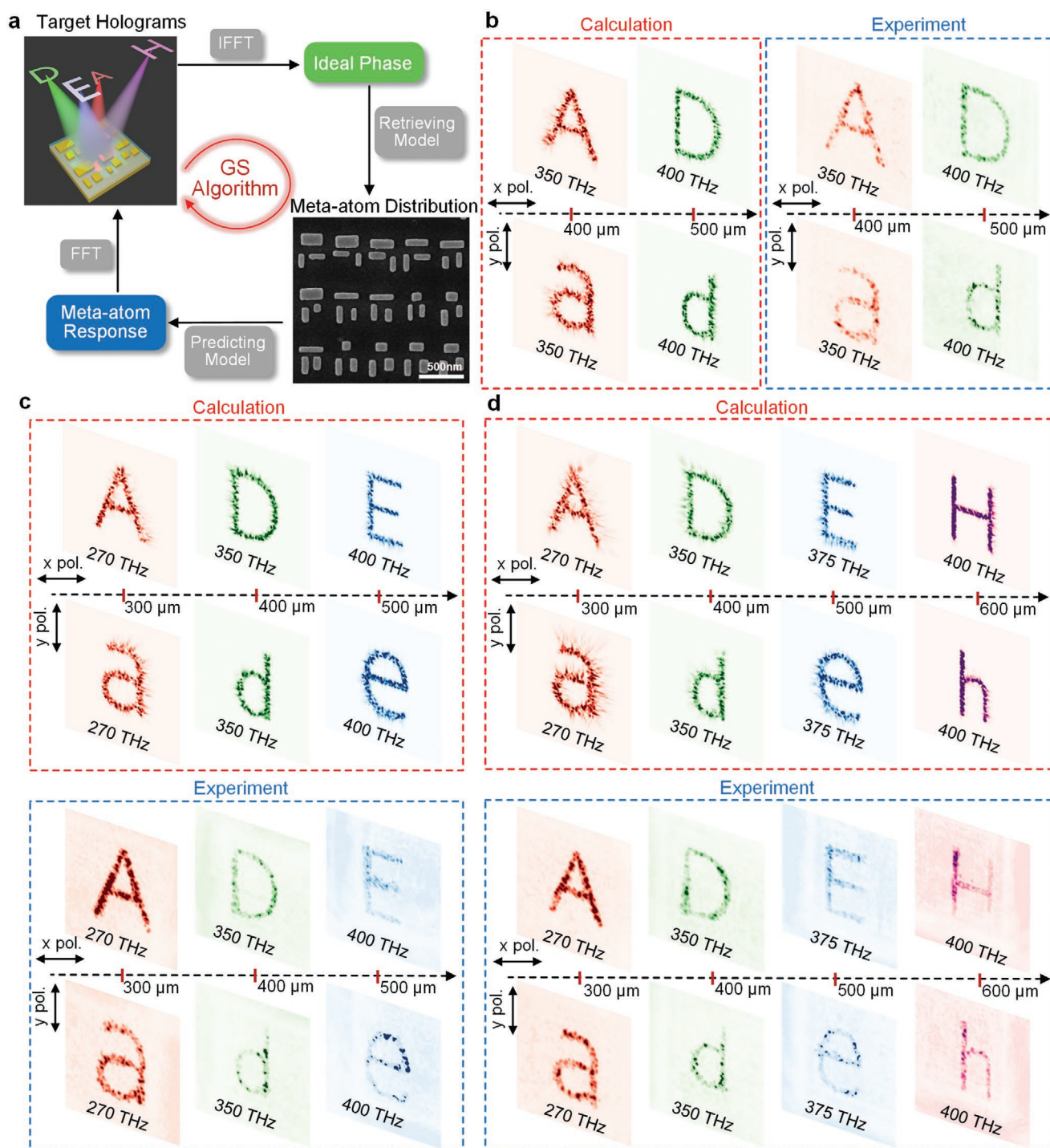MATERIALS**

www.advmat.de

Figure 4. Embedding the statistical learning model in the GS algorithm for multifunctional metasurface holograms. a) Flowchart of the iterative design process, with one scanning electron microscopy image of the fabricated device. b–d) The calculated and experimentally measured hologram images for the two-frequency device (b), the three-frequency device (c), and the four-frequency device (d).

"D", "E", and "H", in either upper or lower case as the target images for different combinations of frequencies and polarizations. The device size of 200 μm × 200 μm and the Fresnel diffraction amendment to FFT are used in the GS algorithm iterations to separate the image plane at 300, 400, 500, and 600 μm, respectively, as annotated in Figure 4b–d. The experimental

measurements agree well with the calculated images by Rayleigh–Sommerfeld diffraction integral, verifying the capability of the proposed design method. Affected by the crosstalk among different functionalities, the signal-to-noise ratio deteriorates as the number of target frequencies increases. It should be noted that the designed reflective holograms solely depend
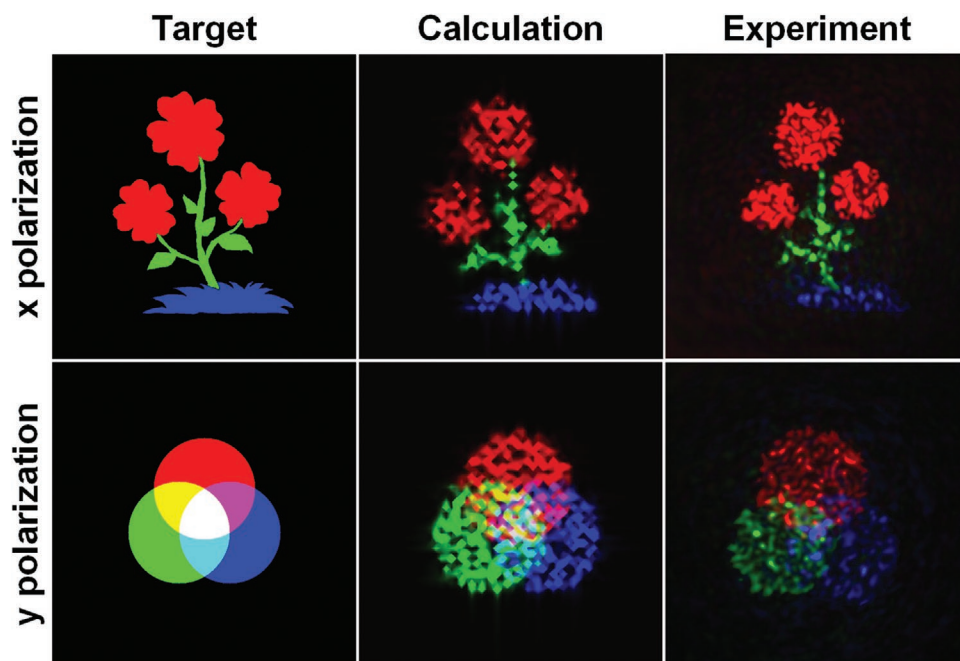
Figure 5. Target, calculated, and experimentally measured multicolor hologram images for both *x*- and *y*-polarizations. The false colors red, green, and blue correspond to 270, 350, and 400 THz, respectively.

on the plasmonic resonance of CRR meta-atoms. Different from the PB phase in a cross-polarized input–output configuration, in our case, the co-polarized reflection cannot be filtered out to improve the image quality. Nevertheless, to the best of our knowledge, the eight distinct images under different combined illumination conditions of two orthogonal linear polarizations and four frequencies are the most independent channels experimentally achieved by a metasurface hologram.

In addition to simple alphabetic letters, we also test our model to design polarization-multiplexed multicolor holograms. As shown in **Figure 5**, the target image is a flower for *x*-polarized incidence and a three-color palette for *y*-polarized incidence. We decompose each image into red, green, and blue components, which represent the working frequencies of 270, 350, and 400 THz, respectively. Using the same design process as described in Figure 4a, a 200 µm × 200 µm hologram is designed and fabricated with the same imaging distance of 500 µm for all frequencies and polarizations. The measured hologram images are demonstrated in Figure 5 together with the target images and theoretically calculated images by diffraction integration. Consistent with the design targets, the metasurface projects two distinct colorful images for two different polarizations, while the resolution of the reconstructed images can be further improved with the increased metasurface size to accommodate more meta-atoms.

3. Conclusions

We have conceptually proposed and experimentally demonstrated the application of statistical machine learning in the design and optimization of complex multifunctional metasurfaces. Mutual information is introduced to quantitatively describe the interdependent optical responses at different frequencies, which provides practical guidelines to estimate the capacity of the design space. Unlike conventional design methods that try to manually decouple different functionalities, the proposed model captures the statistical features among meta-atom structures and their optical responses, enabling us to push the design capacity of the meta-atom to its limit. By embedding the statistical machine-learning model in either gradient-based or nongradient-based optimization, multifunctional metasurfaces can be systematically designed in an end-to-end manner. We successfully realize metasurface focusing lenses and holograms, which show up to eight controllable functionalities for different combinations of working frequencies and polarization states, far beyond the design capability of traditional approaches. It should be noted that the machine-learning model employed in this work is a general inverse design solution that is not limited to CRR meta-atoms based on plasmonic resonances. Other multitarget phase tuning mechanisms like the PB phase or spatial multiplexing can also be included by modifying the model and the corresponding training data. The proposed design framework with embedded statistical machine-learning models opens up a new avenue for automatic, efficient and multiobjective design of complex metasurfaces, which enhances the advantages of metasurfaces over traditional bulk optical components and will significantly accelerate the application of flat optical devices in real-world scenarios.

4. Experimental Section

Dataset Collection and Model Setup: The training data were collected by sampling the design space and numerically calculating the corresponding reflection spectra. The nine design parameters were first sampled independently from a uniform distribution using the Monte

**ADVANCED
SCIENCE NEWS**

www.advancedsciencenews.com

**ADVANCED
MATERIALS**

www.advmat.de

Carlo method, in the range from 40 to 280 nm for the widths (w_1, w_2, and w_3) and lengths (l_1, l_2, and l_3), and from 40 to 120 nm for the gaps (g_1, g_2, and g_3). Then the sampled parameters were filtered to ensure that the CRR structure was confined within the unit cell by a margin of 30 nm or larger in both the horizontal and vertical directions. The qualified designs were fed to commercial simulation package CST Studio Suite to obtain the corresponding reflection spectra using a frequency domain solver. In the simulation, the SiO_2 spacer was modeled as a lossless dielectric with a refractive index of 1.45, and gold was treated by the Drude model. Using the frequency domain solver with a step of 1 THz, the calculated complex spectra for both x- and y-polarizations were discretized into 151 data points, and then decomposed into amplitude and phase components. With the above parameterization, each data pair consisted of a 1×9 design vector and a 4×151 reflection matrix. In total, 70 000 labeled data were collected, among which 65 000 were used as training data, and 5000 were used as test data.

The data collection was automatically performed with the Python programming interface of CST Studio Suite, while all other parts of the design algorithms were also written in Python, including the deep learning models, gradient descent algorithms, and GS algorithms. The neural network models were constructed under the open-source machine-learning framework of PyTorch. In the training process of both predicting and retrieving models, a batch size of 100 and an initial learning rate of 0.001, which was decayed by a scale factor of 0.2 after 50 epochs, were used. An Adam optimizer was used to train the model for 100 epochs with an early stop mechanism.

Device Fabrication: First, a layer of 150 nm Au film was evaporated on a Si substrate with 10 nm Ti as adhesion layer. A 60 nm thick SiO_2 spacer was then deposited using plasma-enhanced chemical vapor deposition (PECVD) technique. Following that, a layer of poly(methyl methacrylate) (PMMA) was spin-coated on the spacer, which was then patterned by the e-beam exposure process. After development, another layer of 50/10 nm thick Au/Ti was evaporated, and the final CRR structures were defined by a lift-off process. Some images of the fabricated devices can be found in Section S9 (Supporting Information).

Supporting Information

Supporting Information is available from the Wiley Online Library or from the author.

Acknowledgements

Conflict of Interest

The authors declare no conflict of interest.

Data Availability Statement

The data that support the findings of this study are available from the corresponding author upon reasonable request.

[1] N. Yu, F. Capasso, *Nat. Mater.* **2014**, *13*, 139.
[2] A. V. Kildishev, A. Boltasseva, V. M. Shalaev, *Science* **2013**, *339*, 1232009.
[3] N. M. Estakhri, A. Alu, *Phys. Rev. X* **2016**, *6*, 041008.
[4] S. Sun, Q. He, S. Xiao, Q. Xu, L. Li, L. Zhou, *Nat. Mater.* **2012**, *11*, 426.
[5] M. Lawrence, D. R. Barton, J. Dixon, J.-H. Song, J. van de Groep, M. L. Brongersma, J. A. Dionne, *Nat. Nanotechnol.* **2020**, *15*, 956.
[6] Z. Shi, A. Y. Zhu, Z. Li, Y.-W. Huang, W. T. Chen, C.-W. Qiu, F. Capasso, *Sci. Adv.* **2020**, *6*, eaba3367.
[7] M. Khorasaninejad, F. Capasso, *Science* **2017**, *358*, eaam8100.
[8] L. Li, K. Yao, Z. Wang, Y. Liu, *Laser Photonics Rev.* **2020**, *14*, 1900244.
[9] X. Ni, A. V. Kildishev, V. M. Shalaev, *Nat. Commun.* **2013**, *4*, 2807.
[10] G. Zheng, H. Mühlenbernd, M. Kenney, G. Li, T. Zentgraf, S. Zhang, *Nat. Nanotechnol.* **2015**, *10*, 308.
[11] S. Jahani, Z. Jacob, *Nat. Nanotechnol.* **2016**, *11*, 23.
[12] N. I. Zheludev, Y. S. Kivshar, *Nat. Mater.* **2012**, *11*, 917.
[13] S. Chen, W. Liu, Z. Li, H. Cheng, J. Tian, *Adv. Mater.* **2020**, *32*, 1805912.
[14] B. Xiong, L. Deng, R. Peng, Y. Liu, *Nanoscale Adv.* **2019**, *1*, 3786.
[15] C. Jung, G. Kim, M. Jeong, J. Jang, Z. Dong, T. Badloe, J. K. Yang, J. Rho, *Chem. Rev.* **2021**, *121*, 13013.
[16] J. Kim, Y. Yang, T. Badloe, I. Kim, G. Yoon, J. Rho, *InfoMat* **2021**, *3*, 739.
[17] I. Kim, J. Jang, G. Kim, J. Lee, T. Badloe, J. Mun, J. Rho, *Nat. Commun.* **2021**, *12*, 3614.
[18] I. Kim, W.-S. Kim, K. Kim, M. A. Ansari, M. Q. Mehmood, T. Badloe, Y. Kim, J. Gwak, H. Lee, Y.-K. Kim, J. Rho, *Sci. Adv.* **2021**, *7*, eabe9943.
[19] B. Xiong, Y. Xu, J. Wang, L. Li, L. Deng, F. Cheng, R. W. Peng, M. Wang, Y. Liu, *Adv. Mater.* **2021**, *33*, 2005864.
[20] R. Jin, L. Tang, J. Li, J. Wang, Q. Wang, Y. Liu, Z.-G. Dong, *ACS Photonics* **2020**, *7*, 512.
[21] F. Aieta, P. Genevet, M. A. Kats, N. Yu, R. Blanchard, Z. Gaburro, F. Capasso, *Nano Lett.* **2012**, *12*, 4932.
[22] M. Decker, I. Staude, M. Falkner, J. Dominguez, D. N. Neshev, I. Brener, T. Pertsch, Y. S. Kivshar, *Adv. Opt. Mater.* **2015**, *3*, 813.
[23] D. Wen, F. Yue, W. Liu, S. Chen, X. Chen, *Adv. Opt. Mater.* **2018**, *6*, 1800348.
[24] Z. Shi, M. Khorasaninejad, Y.-W. Huang, C. Roques-Carmes, A. Y. Zhu, W. T. Chen, V. Sanjeev, Z.-W. Ding, M. Tamagnone, K. Chaudhary, *Nano Lett.* **2018**, *18*, 2420.
[25] S. Wang, P. C. Wu, V.-C. Su, Y.-C. Lai, C. H. Chu, J.-W. Chen, S.-H. Lu, J. Chen, B. Xu, C.-H. Kuan, T. Li, S. Zhu, D. P. Tsai, *Nat. Commun.* **2017**, *8*, 187.
[26] W. T. Chen, A. Y. Zhu, V. Sanjeev, M. Khorasaninejad, Z. Shi, E. Lee, F. Capasso, *Nat. Nanotechnol.* **2018**, *13*, 220.
[27] E. Maguid, I. Yulevich, D. Veksler, V. Kleiner, M. L. Brongersma, E. Hasman, *Science* **2016**, *352*, 1202.
[28] Y.-W. Huang, W. T. Chen, W.-Y. Tsai, P. C. Wu, C.-M. Wang, G. Sun, D. P. Tsai, *Nano Lett.* **2015**, *15*, 3122.
[29] O. Avayu, E. Almeida, Y. Prior, T. Ellenbogen, *Nat. Commun.* **2017**, *8*, 14992.
[30] S. Molesky, Z. Lin, A. Y. Piggott, W. Jin, J. Vucković, A. W. Rodriguez, *Nat. Photonics* **2018**, *12*, 659.

**ADVANCED
SCIENCE NEWS**

www.advancedsciencenews.com

**ADVANCED
MATERIALS**

www.advmat.de

[31] A. Y. Piggott, J. Lu, K. G. Lagoudakis, J. Petykiewicz, T. M. Babinec, J. Vučković, *Nat. Photonics* **2015**, *9*, 374.

[32] L. Su, A. Y. Piggott, N. V. Sapra, J. Petykiewicz, J. Vuckovic, *ACS Photonics* **2018**, *5*, 301.

[33] H. Chung, O. D. Miller, *Opt. Express* **2020**, *28*, 6945.

[34] M. Mansouree, H. Kwon, E. Arbabi, A. McClung, A. Faraon, A. Arbabi, *Optica* **2020**, *7*, 77.

[35] M. D. Huntington, L. J. Lauhon, T. W. Odom, *Nano Lett.* **2014**, *14*, 7195.

[36] J. Hu, C.-H. Liu, X. Ren, L. J. Lauhon, T. W. Odom, *ACS Nano* **2016**, *10*, 10275,

[37] Y. LeCun, Y. Bengio, G. Hinton, *Nature* **2015**, *521*, 436.

[38] K. T. Butler, D. W. Davies, H. Cartwright, O. Isayev, A. Walsh, *Nature* **2018**, *559*, 547.

[39] Y. Xu, X. Zhang, Y. Fu, Y. Liu, *Photonics Res.* **2021**, *9*, B135.

[40] W. Ma, Z. Liu, Z. A. Kudyshev, A. Boltasseva, W. Cai, Y. Liu, *Nat. Photonics* **2021**, *15*, 77.

[41] I. Malkiel, M. Mrejen, A. Nagler, U. Arieli, L. Wolf, H. Suchowski, *Light: Sci. Appl.* **2018**, *7*, 60.

[42] W. Ma, F. Cheng, Y. Liu, *ACS Nano* **2018**, *12*, 6326.

[43] D. Liu, Y. Tan, E. Khoram, Z. Yu, *ACS Photonics* **2018**, *5*, 1365.

[44] J. Peurifoy, Y. Shen, L. Jing, Y. Yang, F. Cano-Renteria, B. G. DeLacy, J. D. Joannopoulos, M. Tegmark, M. Soljačić, *Sci. Adv.* **2018**, *4*, eaar4206.

[45] L. Pilozzi, F. A. Farrelly, G. Marcucci, C. Conti, *Commun. Phys.* **2018**, *1*, 57.

[46] I. Sajedian, J. Kim, J. Rho, *Microsyst. Nanoeng.* **2019**, *5*, 27.

[47] Z. Liu, D. Zhu, S. P. Rodrigues, K.-T. Lee, W. Cai, *Nano Lett.* **2018**, *18*, 6570.

[48] S. So, J. Rho, *Nanophotonics* **2019**, *8*, 1255.

[49] J. Jiang, D. Sell, S. Hoyer, J. Hickey, J. Yang, J. A. Fan, *ACS Nano* **2019**, *13*, 8872.

[50] W. Ma, F. Cheng, Y. Xu, Q. Wen, Y. Liu, *Adv. Mater.* **2019**, *31*, 1901111.

[51] W. Ma, Y. Liu, *Sci. China: Phys., Mech. Astron.* **2020**, *63*, 284212.

[52] N. J. Dinsdale, P. R. Wiecha, M. Delaney, J. Reynolds, M. Ebert, I. Zeimpekis, D. J. Thomson, G. T. Reed, P. Lalanne, K. Vynck, O. L. Muskens, *ACS Photonics* **2021**, *8*, 283.

[53] Z. Liu, D. Zhu, K. T. Lee, A. S. Kim, L. Raju, W. Cai, *Adv. Mater.* **2020**, *32*, 1904790.

[54] D. Zhu, Z. Liu, L. Raju, A. S. Kim, W. Cai, *ACS Nano* **2021**, *15*, 2318.

[55] Z. A. Kudyshev, A. V. Kildishev, V. M. Shalaev, A. Boltasseva, *Appl. Phys. Rev.* **2020**, *7*, 021407.

[56] J. Jiang, J. A. Fan, *Nano Lett.* **2019**, *19*, 5366.

[57] G. Yoon, J. Kim, J. Mun, D. Lee, K. T. Nam, J. Rho, *Commun. Phys.* **2019**, *2*, 129.

[58] F. Aieta, M. A. Kats, P. Genevet, F. Capasso, *Science* **2015**, *347*, 1342.

[59] A. Kraskov, H. Stögbauer, P. Grassberger, *Phys. Rev. E* **2004**, *69*, 066138.